Research Article

ADVANCED PHOTONICS

Microscale fiber photoacoustic spectroscopy for *in situ* and real-time trace gas sensing

Jun Ma,[a,b,†] Enbo Fan,[a,b,†] Haojie Liu,[a,b,†] Yi Zhang,[c] Cong Mai,[d] Xin Li,[d] Wei Jin,[e,*] and Bai-Ou Guan[a,b,*]

[a]Jinan University, Institute of Photonics Technology, Guangdong Provincial Key Laboratory of Optical Fiber Sensing and Communications, Guangzhou, China

[b]Jinan University, College of Physics & Optoelectronic Engineering, Guangzhou, China

[c]Jinan University, College of Life Science and Technology, Guangzhou, China

[d]Guangdong Provincial People's Hospital, Southern Medical University, Guangdong Academy of Medical Sciences, Department of Critical Care Medicine, Guangzhou, China

[e]The Hong Kong Polytechnic University, Department of Electrical and Electronic Engineering, Hong Kong, China

Abstract. Miniaturized laser spectroscopy capable of *in situ* and real-time ppb-level trace gas sensing is of fundamental importance for numerous applications, including environment monitoring, industry process control, and biomedical diagnosis. Benchtop laser spectroscopy systems based on direct absorption, photoacoustic, and Raman effects exhibit high sensitivity but face challenges for *in situ* and real-time gas sensing due to their bulky size, slow response, and offline sampling. We demonstrate a microscale high-performance all-fiber photoacoustic spectrometer integrating the key components, i.e., the photoacoustic gas cell and the optical microphone, into a single optical fiber tip with a diameter of 125 μm. Without a long optical path to enhance the light–gas interaction, the fiber-tip gas cell with acoustic-hard boundary tightly confines and amplifies the local photoacoustic wave, compensating for the sensitivity loss during miniaturization. This localized acoustic wave is demodulated by high-sensitivity fiber-optic interferometry, enabling a ~9 ppb detection limit for acetylene gas approaching the benchtop system. The microscale fiber spectrometer also exhibits a short response time of ~18 ms and a subnanoliter sample volume, not only suitable for routine real-time *in situ* trace gas measurement but also inspiring new applications such as two-dimensional gas flow concentration mapping and *in vivo* intravascular blood gas monitoring as showcased.

Keywords: optical fiber sensors; photoacoustic spectroscopy; acoustic sensing; trace gas detection.

Received Jul. 21, 2024; revised manuscript received Oct. 19, 2024; accepted for publication Nov. 20, 2024; published online Dec. 17, 2024.

[DOI: 10.1117/1.AP.6.6.066008]

1 Introduction

Miniaturized spectroscopy has been a burgeoning analytical technique allowing on-site analysis of diverse chemical compositions, moving the purely laboratory-limited test to broad scenarios ranging from the deep ocean to far-reach aerospace.[1–3] The recently emerging fields such as lithium battery health assessment in new energy automobiles and intravascular diagnosis in biomedicine require minimal invasion and small sampling volume, also motivating the development of miniaturized spectroscopy. For gas phase analysis in chemical, atmospheric, and biomedical science, the ideal miniaturized spectroscopy is expected to possess high sensitivity, fast response, small footprint, and little or no gas consumption. Over the past decades, laser spectroscopy techniques such as cavity ring-down spectroscopy (CRDS), Raman spectroscopy, direct absorption spectroscopy (DAS), and photothermal spectroscopy have drawn great interest for trace gas detection because of their high sensitivity, no gas consumption, continuous monitoring, and long lifetime.[4–7] These techniques can deliver ultralow detection limit down to parts per billion (ppb) to parts per trillion (ppt) level, or equivalently, an analyte absorption coefficient of less than 10^{-9} cm^{-1},

*Address all correspondence to Wei Jin, wei.jin@polyu.edu.hk; Bai-Ou Guan, tguanbo@jnu.edu.cn

†These authors contributed equally to this work.

while they are commonly embodied in benchtop laboratory spectroscopy systems characterized by bulky optical components, highly reflective mirrors, and long path lengths. To remove the bulky free-space optics and open-path gas cell, hollow-core bandgap or antiresonant fibers with an air core size of several to tens of micrometers are utilized to tightly confine both the gas molecules and the pump light.[8–10] However, a long piece of optical fiber, typically tens of centimeters, is necessary to accumulate sufficient light phase change in the fiber for ppb-level gas sensing. In addition, the gas diffusion through the small-core fiber over a long distance is time-consuming if no external pressure is applied to the fiber opening, thus hindering the *in situ* and real-time applications. On-chip spectroscopy is an alternative solution to reduce the device form factor and can be potentially integrated as arrays for parallel analysis of multiple gas species.[11–14] However, simple downscaling of the spectroscopy components to the chip scale inevitably weakens the light–matter interaction caused by the short waveguide and limits the performance to parts per million (ppm) level. As these pure optical techniques rely on the detection of the accumulated light intensity or phase change induced by the gas absorption, either highly reflective mirrors or long gas cells are indispensable to increase the optical path for high performance.

Photoacoustic spectroscopy (PAS) measuring acoustic waves emitted from gas molecules excited by modulated or pulsed light arguably holds the potential to pursue extremely compact gas sensors, considering its path length-independent sensitivity.[15] The PAS systems based on electrical microphones such as the piezoelectric crystal, MEMS transducer, and quartz tuning fork can achieve ppb-level gas detection limit.[16–19] Due to the relatively low sensitivity of the microphone, resonant gas cells with dimensions close to the acoustic wavelengths are integrated to amplify the acoustic signals, which greatly increases the size of the current PAS systems. Recently, electrical microphones have been replaced by optical microphones based on the silicon cantilever and graphene diaphragm with a low acoustic detection limit down to the micropascal level (μPa/Hz$^{1/2}$).[20–24] However, these optical microphones still have a large size of several millimeters because their acoustic sensitivity severely degrades with the size reduction of the cantilever or diaphragm and thereby are routinely inserted into a bulky gas cell in the same configuration as the electrical ones for gas sensing. This makes the current PAS systems still deviate far from a real miniature footprint and suffer a slow gas response, since the equilibrium of gas diffusion in the large gas cell can take up to several minutes.[25–27] Recently, patterning optical fiber facets with nanostructures has drawn great interest because optical fibers offer a convenient platform for the realization of miniature and flexible in-fiber devices for narrow space and long-distance applications. Phase/intensity modulation,[28] plasmon–atom interaction,[29] and *in situ* SERS sensing[30] have been realized on the fiber tip. Three-dimensional (3D) direct laser writing has also been employed for manufacturing miniature polymer or inorganic glass cavities on the endface of a standard telecom fiber for organic vapor sensing. By measuring the refractive index changes of the vapor/gas trapped inside the cavity, only ppm-level ethanol vapor detection can be achieved and the gas specificity is also a concern.[31,32] Therefore, it remains a great challenge for laser spectroscopy to develop a fully miniaturized spectrometer with microscale size, high sensitivity, and fast response for *in situ* and real-time trace gas sensing, especially for lithium battery health monitoring and intravascular diagnosis desiring minimal invasiveness.

Here, we propose a microscale all-in-one fiber photoacoustic spectrometer (FPAS) that detects the local acoustic waves emitted from light-excited gas molecules inside the fiber tip Fabry–Perot (F–P) cavity. The F–P cavity with a diameter of 125 μm and a length of 60 μm serves as both the optical microphone and the gas cell, shrinking the device footprint for over 2 orders of magnitude compared with previous systems, and achieves a ppb-level detection limit with no need for a bulky resonant gas cell. To address the trade-off between the sensitivity and footprint, a laser-patterned thin polymer membrane that exhibits an acoustic sensitivity scaling down with the diameter a following a dependence of a^2 instead of a^4 as that for the normal plate is employed to build the fiber F–P microphone. Meanwhile, a gas cell constructed with a rigid silica capillary is used to confine and amplify the locally generated acoustic waves. This local acoustic amplification compensates for the sensitivity loss caused by the reduction in the membrane diameter and results in a size-independent photoacoustic (PA) response. Both the pump and probe light beams are directly delivered through the same fiber for the excitation and detection of the PA signal, avoiding bulky free-space optics for the light delivery. In combination with the high-precision fiber-optic interferometry to demodulate the membrane deflection of the microphone induced by the PA waves, the microscale FPAS achieves a detection limit of ~9 ppb for acetylene (C_2H_2) gas (averaging time of 200 s) approaching that of the benchtop system. Besides the low detection limit, the microscale FPAS exhibits a short response time of ~18 ms, a high spatial resolution of ~160 μm, and a small sample volume of sub-nanoliter, improving the spatial and temporal resolutions by more than 2 to 3 orders of magnitude and reducing the sample volume by 3 to 4 orders of magnitude. Two-dimensional (2D) mapping of the concentration distribution in the gas flow, monitoring of released carbon dioxide (CO_2) from living yeast cells, and *in vivo* recording of the dynamic dissolved CO_2 concentration in the rat tail vessel under the hypoxic or hypercapnic condition are showcased.

2 Results

2.1 Theory of the Microscale FPAS

For the all-in-one FPAS as shown in Fig. 1(a), the gas molecules diffuse into the silica capillary, absorb the pump light, and generate acoustic waves. The acoustic waves are tightly confined by the rigid capillary wall that acts as a hard acoustic boundary [inset of Fig. 1(a)] and exhibit a more than 1 order of magnitude higher pressure level compared with the free-space spreading-out PA waves. These locally amplified acoustic waves deform the thin elastic membrane behaving as a mechanical oscillator at the capillary opening. Because the membrane also serves as a reflective mirror and forms an F–P cavity with the facet of the single-mode fiber (SMF) tip, the acoustic-wave-induced membrane deformation can be demodulated in high sensitivity with a narrowband probe light based on the principle of fiber-optic interferometry. The scheme of the PA wave excitation and demodulation is shown in Fig. 1(b), where the wavelength of the pump light is slowly scanned across the gas absorption line and the intensity is modulated sinusoidally. These locally excited PA waves after the amplification in the tiny cavity deform the membrane and cause the spectral shift in the reflection spectrum of the F–P cavity. The spectral shift is converted to the intensity change of the probe light and subsequently to electrical

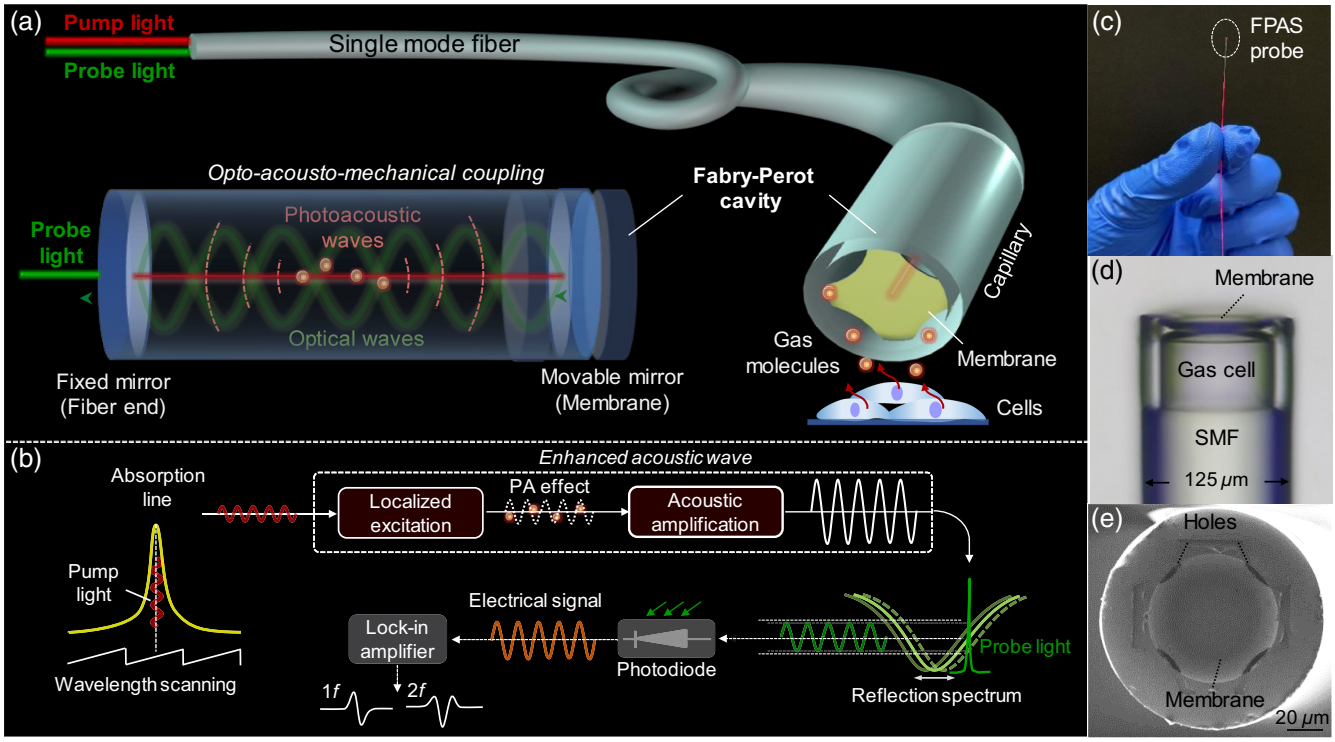

Fig. 1 (a) Schematic of the microscale fiber photoacoustic spectrometer (FPAS). Inset: opto-acoustic-mechanical coupling inside the F–P cavity. The fiber end facet and the membrane are two reflective mirrors, which form the F–P cavity with the silica capillary. The acoustic wave generated during the relaxation of the excited gas molecules by the pump light is confined inside the cavity. The localized acoustic waves drive the membrane to vibrate, which induces the intensity change in the reflected probe light. (b) Signal demodulation scheme for the FPAS. (c) Photograph and (d) microscopic image of the FPAS. (e) SEM image of the fiber end facet with the membrane after the laser patterning. SMF, single mode fiber; PA, photoacoustic; 1f and 2f, the first- and second-harmonic signals.

signals by a photodiode (PD). The fundamental (1f) or second-harmonic (2f) signals are acquired using a lock-in amplifier to retrieve the gas concentration.

The PA response of the FPAS to gas molecules can be described by

$$S = M \cdot C_{\text{cell}} \cdot P_0 \cdot \alpha \cdot C + S_b, \tag{1}$$

where M is the acoustic sensitivity depending on the membrane mechanical behavior, C_{cell} is the constant of the gas cell accounting for the PA wave generation and local amplification, P_0 is the pump power for the PA wave excitation, α is the absorption coefficient of the gas, C is the gas concentration, and S_b is the background noise. The acoustic sensitivity M can be derived from the mechanical deformation of the membrane when subjected to unit acoustic pressure. For an elastic thin diaphragm with a clamped periphery, the small out-of-plane displacement $u(r,t)$ of the diaphragm under a sinusoidal acoustic wave with the pressure amplitude p_0 can be described by the motion equation as[33]

$$\left(h\rho\frac{\partial^2}{\partial t^2} + D\nabla^4 - h\sigma\nabla^2\right)u(r,t) = p_0 e^{jwt}, \tag{2}$$

where h is the diaphragm thickness, ρ is the diaphragm density, σ is the residual stress, D is the flexural rigidity equal to $Eh^3/12(1-v^2)$, E is the Young's modulus, v is the Poisson's ratio, and w is the angular frequency of the acoustic wave. If the effect of residual stress dominates that from the flexural rigidity D, the second term in the left hand of Eq. (2) can be ignored, and the diaphragm is modeled as a membrane instead of a plate. Then, solving Eq. (2) can obtain a simple analytic approximation for the displacement of an edge-clamped membrane as $u(r,t) = p_0 e^{jwt}(a^2 - r^2)/4h\sigma$ if the damping effect is negligible. The displacement at the membrane center $u(0,t)$ under unit pressure, i.e., acoustic sensitivity, increases with the reduction in the thickness h and scales down with the diameter a following a relationship of a^2 instead of a^4 as that for the plate.[34] Therefore, an elastic membrane with a nanoscale thickness is selected to build the miniature fiber-optic F–P microphone to achieve high acoustic sensitivity with a small form factor. Here, the damping effects from both the air cavity and the holey membrane are neglected to obtain a simple formula for the acoustic sensitivity of the membrane. An equivalent circuit using the lumped elements is adopted to study these damping effects on the acoustic sensitivity of the membrane at different frequencies in the next section.

The PA wave excited by the modulated pump light drives the membrane to vibrate; the distribution of the PA wave pressure inside the F–P cavity can be described by[35]

$$p(\boldsymbol{r}, w) = \sum_j A_j(w) p_j(\boldsymbol{r}), \tag{3}$$

$$A_j(w) = -\frac{iw}{w_j^2} \frac{\alpha(\gamma-1) \iiint p_j^*(\boldsymbol{r}) I(\boldsymbol{r}, w) \mathrm{d}V}{V_c \left(1 - \frac{w^2}{w_j^2} - iw/(w_j Q_j)\right)}, \tag{4}$$

where $p_j(\boldsymbol{r})$ is the j'th normal mode of the cavity; $A_j(w)$ is the amplitude of $p_j(\boldsymbol{r})$; Q_j and w_j are the quality factor and the angular frequency of the j'th normal mode, respectively; $I(\boldsymbol{r}, w)$ is the spatial distribution of the pump light intensity; γ is the ratio of the specific heats; and V_c is the volume of the F–P cavity. As the cavity has a radius much smaller than the acoustic wavelength, it can be regarded as a non-resonant gas cell ($w_j \approx 0$) featuring a uniform distribution of the pressure in the cavity. By assuming that the pump light beam size is much smaller than the cavity inner diameter and neglecting the light diffraction along the axis, the full expression $p(\boldsymbol{r}, w)$ can then be simplified as[36]

$$p(\boldsymbol{r}, w) \propto \alpha P_0 \frac{(\gamma-1)L}{V_c} \frac{\tau_1}{\sqrt{1+(w\tau_1)^2}} \frac{w\tau_2}{\sqrt{1+(w\tau_2)^2}}, \tag{5}$$

$$\tau_1 = \frac{R^2}{5.78 D_T} \quad \tau_2 = \frac{4\sqrt{\gamma} V_c}{3 A_g v}, \tag{6}$$

where L is the length of the cavity, τ_1 is the thermal damping time of the gas molecules in the cavity, τ_2 is the time constant accounting for the damping effect caused by the gas and heat flows, R is the cavity radius equal to half of the membrane diameter a, D_T is the thermal diffusivity of the target gas, A_g is the area of the holes, and ν is the sound velocity in the gas. For the cylindrical cavity, the cavity volume $V_c = \pi R^2 L = \pi a^2 L/4$. Then, the simplified Eq. (5) suggests that the PA wave pressure $p(\boldsymbol{r}, w)$ is proportional to a^{-2}. Considering the aforementioned analytic approximation for the displacement of an edge-clamped membrane, the acoustic sensitivity of the membrane is proportional to a^2. Then, the PA response of the FPAS is actually independent of the cavity diameter, which facilitates the miniaturization of the device without the expense of gas sensitivity.

2.2 Acoustic Response

Figures 1(c) and 1(d) show the photograph and the microscopic image of the fiber-tip structure of the FPAS. The silica capillary has a bore diameter of 75 μm and an outer diameter compatible with the SMF with a diameter of 125 μm. The opening of the capillary is covered with a ~200-nm-thick polymer membrane. The F–P cavity formed by the SMF end facet and the membrane functions as both the micro gas cell and the optical microphone. The reflection spectra for the cavity with membranes of different thicknesses show periodic fringes with a slowly varying envelope (Supplementary Material Note 1). As the FPAS detects photoacoustic waves based on the F–P interferometry, the refractive index contrast between the gas and the cavity mirrors, i.e., the fiber end facet and the membrane, can change the light reflectivity of the mirror. Fortunately, even pure gas, such as C_2H_2, can only change the air refractive index by less than 0.02% at room temperature and in the atmosphere, which is negligible to the refractive index contrast between the gas and the cavity mirrors with a refractive index of ~1.45 for the fiber endface and ~1.52 for the membrane. Figure 1(e) shows the scanning electron microscopy (SEM) image of the fiber tip after the femtosecond (fs) laser patterning of the membrane with holes. As the PA response of the FPAS is dependent on the acoustic sensitivity M according to Eq. (1), a narrowband probe light from a tunable laser is used to characterize the acoustic sensitivity M by recording the intensity change of the reflected light induced by the acoustic waves. The wavelength of the probe light is tuned to the quadrature point of the FPAS reflection spectrum for maximum sensitivity. The FPAS exhibits a flat acoustic response in the frequency range from 1 to 20 kHz, as shown in Fig. 2(a). Further characterization of the high-frequency response is hindered by the limited bandwidth of the calibration microphone used. By measuring the noise floor,

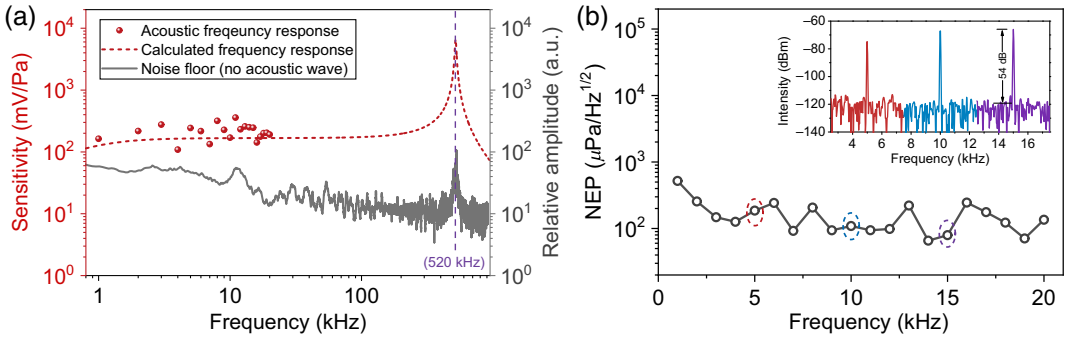

Fig. 2 (a) Measured response of the FPAS to acoustic waves from 1 to 20 kHz and calculated frequency response based on the equivalent circuit using the lumped elements. The resonant frequency is located at 520 kHz, as observed from the measured noise floor in the absence of an applied acoustic wave. (b) NEP of the FPAS was measured at different frequencies from 1 to 20 kHz. Inset: frequency responses at 5, 10, and 15 kHz. At the frequency of 15 kHz, SNR is estimated to be 54 dB for an acoustic pressure of 280 MPa.

it is found that the thermal-mechanical noise is amplified by the mechanical resonance of the membrane and peaks at the frequency of 520 kHz. The measured results are fitted by the calculated frequency response based on the equivalent circuit using the lumped elements (Supplementary Material Note 2). If the FPAS works at nonresonant frequency drift, its broad bandwidth can alleviate the signal fading problem caused by the resonant frequency drift existing for the tuning fork or the cantilever-based PAS systems.[37,38] During the test, no servo-control of the probe light wavelength is needed to lock the operation point of the FPAS at the quadrature point. The wavelength shift of the FPAS is found to be less than 0.1 nm over a duration of 3 h, ~2% of the linear working range of the FPAS (Supplementary Material Note 3). This spectral stability is a result of the laser-patterned holes in the membrane. The holes acting as a high-pass filter significantly reduce the static and slow environmental pressure fluctuations. The noise equivalent pressure (NEP) of the FPAS is characterized by the signal-to-noise ratio (SNR) of the measured acoustic response, as shown in Fig. 2(b). At the frequency of 15 kHz, an SNR of ~54 dB for an acoustic pressure of 280 mPa corresponds to an NEP of ~80 μPa/Hz$^{1/2}$ [inset of Fig. 2(b)]. This value is comparable with the previous fiber-optic F–P acoustic sensor employing a 6-mm-diameter diaphragm,[39] thanks to the high compliance of the nanometer-thick stretched membrane (Supplementary Material Note 4).

2.3 Photoacoustic Gas Response

To verify the size-independent PA response, FPASs with different F–P cavity diameters of 150, 75, and 25 μm are prepared and characterized with the experimental setup shown in Fig. 3(a). The second-harmonic (2f) component of the PA signal from the C_2H_2 gas molecules is acquired based on the wavelength modulation scheme (WMS). Pump light from a distributed feedback (DFB) laser at 1532.8 nm is slowly wavelength-scanned across the C_2H_2 absorption line P(13) with absorbance α of ~1.1 cm^{-1} by controlling the laser temperature. Simultaneously, the laser wavelength is sinusoidally modulated by varying the laser driving current. The gas molecular absorption spectrum of the FPAS is obtained by recording the corresponding acoustic signals that are converted into electrical signals by the microphone during the wavelength scanning of the pump laser wavelength. The power of the pump light for the PA gas measurement is amplified by an erbium-doped optical fiber amplifier (EDFA) from 10 to 50 mW. The measured PA responses from the FPASs with different cavity diameters at a modulation frequency of 7 kHz are compared in Fig. 3(b), with the x axis standing for the wavelength and the y axis for the 2f signal. The 2f signal from the FPAS remains almost unchanged as the cavity diameter reduces from 150 to 75 μm, even though the acoustic response reduces ~4 times (Supplementary Material Note 5). This size-independent PA response as a result of the locally amplified

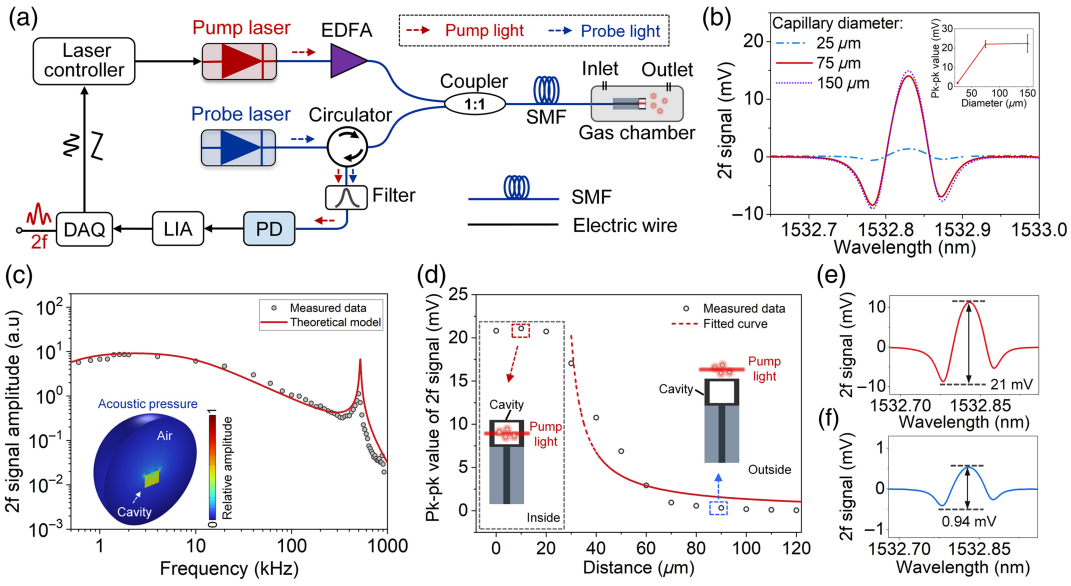

Fig. 3 (a) Schematic diagram of the experimental setup for photoacoustic gas sensing. The EDFA amplified pump laser at 1532.8 nm and the probe light at 1550 nm are combined by the coupler and delivered to the FPAS fiber tip. After filtering off the residual pump light, the probe light is received by a PD. The signal from the PD is analyzed by the lock-in amplifier (LIA). The pump light is wavelength-modulated by the laser controller. (b) Measured second-harmonic (2f) signals for FPASs with different cavity diameters. Inset: pk-pk value of the 2f signal as a function of the cavity diameter. Three samples are tested for each cavity diameter. (c) Relative pk-pk value of the 2f signal in the frequency range from 0.6 kHz to 1 MHz acquired from the experiment and the finite-element simulation. Inset: simulated local photoacoustic waves confined in the cavity through the simulation. (d) Pk-pk value of 2f signal for the pump light at different locations with a step size of 10 μm. Inset: schematic of the 2f signal excitation with the pump light inside and outside the cavity. (e), (f) 2f signals for the pump light at locations as indicated by the dashed boxes in panel (d). DAQ, data acquisition unit; SMF, single-mode fiber.

acoustic pressure inside the cavity is in accordance with the previous theoretical prediction. As the cavity diameter further goes down to 25 μm, however, the PA response reduces rapidly. This is caused by the increased acoustic loss suffered by the cavity with a smaller diameter because the cavity size is close to the viscous and thermal boundary layer thickness (Supplementary Material Note 6). Therefore, a silica capillary with a bore diameter of 75 μm is selected for constructing the F–P cavity to optimize the sensing performance of the FPAS.

The sinusoidal modulation frequency of the pump light wavelength is tuned from 0.6 kHz to 1 MHz to determine the frequency with the optimum SNR. The recorded peak-to-peak (pk-pk) values of the 2f signals are plotted in Fig. 3(c). At the frequency below 1 kHz, the signal amplitude reduces because the holes in the membrane filter off the low-frequency PA waves. As the frequency increases, the PA signal amplitude gradually decreases due to its inverse proportion to the modulation frequency as $w\tau_1$, $w\tau_2 \gg 1$. The peak at the frequency of 520 kHz results from the mechanical resonance of the membrane. The theoretical study of the locally generated PA waves as well as the total PA response of the FPAS is performed (Supplementary Material Note 6), showing good agreement with the measured data, as shown in Fig. 3(c). As the signal amplitude reduces slightly faster with the frequency than the noise level, the SNR at the resonant frequency is found to be lower than that at 14 kHz. Therefore, half the frequency, i.e., 7 kHz, is selected as the optimal modulation frequency of the pump light.

Using the finite-element simulation (see Supplementary Material Note 6), the spatial distribution of the locally generated PA waves confined in the cavity is shown in the inset of Fig. 3(c). To experimentally verify the PA signal amplification by the microscale cavity, the pump light is delivered into the cavity from the sidewall via a second SMF, instead of through the FPAS fiber end facet. The pump light travels through the transparent silica wall of the cavity and moves from the cavity inside to the outside by translating the fiber with a step size of 10 μm. The PA signal amplitude is ~20 times stronger when the pump light passes through the cavity compared with the case that the pump light leaves the cavity, as shown in Figs. 3(d)–3(f). Once the pump beam moves outside the cavity, the amplitude of the PA signal gradually decays with the distance between the membrane and the pump light beam due to the spread of the generated PA wave into the free space. The measured data for the beam outside the cavity agree with the fitted curve denoting an inverse proportion of the pressure amplitude to the distance between the pump beam and the cavity. This local enhancement of the PA signal by the silica cavity is critical to achieving a high sensitivity for the FPAS with a microscale form factor.

2.4 NEC and Response Time

The pk-pk value of the 2f signal from the FPAS linearly increases with the pump power from 10 to 50 mW, and the noise floor remains nearly unchanged, as shown in Fig. 4(a), thanks to

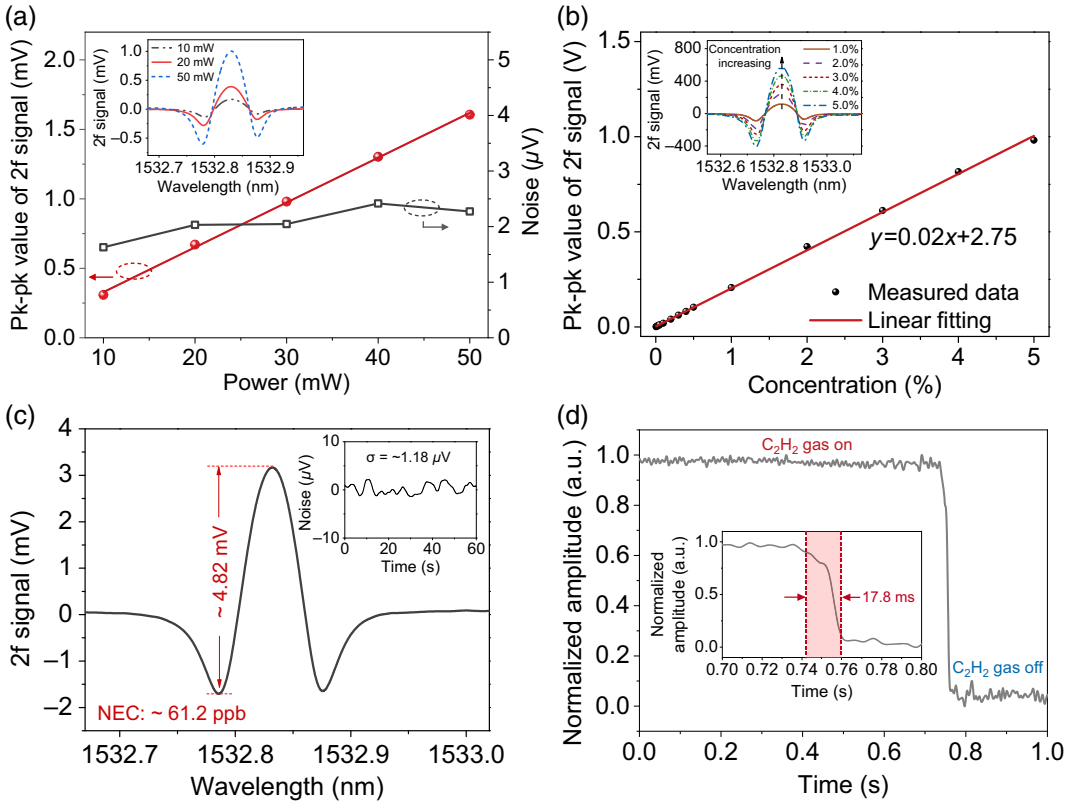

Fig. 4 (a) Dependence of the second-harmonic (2f) signal and the noise floor on the pump power. Inset: 2f signals at different pump powers. (b) Pk-pk value of the 2f signal as a function of the gas concentration. Inset: 2f signals at different gas concentrations. (c) Measured 2f signal to a C_2H_2 gas concentration of 250 ppm. Inset: noise floor. (d) Temporal response as the C_2H_2 gas is switched on and off. Inset: response in the duration from 0.7 to 0.8 s.

the transparency of the membrane to the pump light. This allows the delivery of the pump light together with the probe light through the same fiber in the FPAS instead of using two separate fibers to reduce the background signal caused by the pump light absorption. Further increase of the pump power is found to be accompanied by the raised background signal caused by the membrane absorption, which hinders the further improvement of the SNR. By continuously monitoring the FPAS output for 2 h when the pump light wavelength is tuned away from the gas absorption line, the noise equivalent concentration (NEC) of the FPAS after performing the Allan deviation analysis is ~9 ppb at the pump power of ~50 mW at an averaging time of 200 s (Supplementary Material Note 7). The 2f signals for the C_2H_2 gas with different concentrations are also recorded. As shown in Fig. 4(b), the FPAS exhibits a linear response up to the gas concentration of 5%, corresponding to a dynamic range of $\sim 5 \times 10^6$ (Supplementary Material Note 8). For the C_2H_2 gas with a concentration of 250 ppm, the NEC of the FPAS can be estimated to be ~61.2 ppb based on the measured pk-pk value of the 2f signal and the noise floor, as shown in Fig. 4(c). To avoid the influence of the pump laser power and the gas species such as the C_2H_2 and CO_2 featuring absorption lines of different wavelengths and intensities on the evaluation of the system performance, the normalized noise equivalent absorption coefficient (NNEA) is calculated by normalizing the NEC with the gas absorption coefficient α, the pump laser power P_0, and the detection bandwidth Δf. For the FPAS with an NEC of ~61.2 ppb for C_2H_2 gas and the lock-in amplifier bandwidth of 0.3 Hz, the corresponding NNEA is $\sim 6.1 \times 10^{-9}$ cm^{-1} W Hz$^{-1/2}$. To study the temporal response of the FPAS, we continuously monitor the peak value of the 2f signal while quickly cutting off the C_2H_2 gas flow. The response time as estimated from the temporal response of the FPAS in Fig. 4(d) is ~18 ms, about 2 to 3 orders of magnitude shorter than that of the previous PAS systems, due to the significantly reduced cavity length. The measured response time is still longer than the theoretical diffusion time (~1.8 ms) for a cavity length of 60 μm (Supplementary Material Note 9), which is mainly caused by the switching speed of the gas flow in the test.

2.5 Mapping of Gas Flow and in situ Monitoring of Fermentation Process

To verify the fast response and high spatial resolution of the FPAS, 2D mapping of the concentration distribution in the CO_2 gas flow by scanning the fiber tip with the translation stage is performed, as shown in Fig. 5(a). The pump laser at the wavelength of 1578.67 nm is used here for the CO_2 measurement. As shown in Fig. 5(b), the diffusion process of the gas flow can be clearly observed. By increasing the flow rate to form a sharp gas boundary between the gas and the surrounding air, the spatial resolution can be estimated to be ~160 μm from the edge spread function (ESF) and the corresponding point spread function (PSF), as plotted in Fig. 5(c). The resolution is larger than the FPAS cavity diameter, which may be attributed to the gas diffusion at the boundary of the gas flow.

2.6 In situ Monitoring of Fermentation Process in Yeast Solution

The FPAS is further employed to monitor the fermentation process in the glucose-mixed yeast solution, as shown in Fig. 5(d). A test tube and a glass capillary are used to mimic the mini-bioreactors, as shown in Figs. 5(e) and 5(f). The temporal variation of the CO_2 gas concentration during the fermentation is shown in Fig. 5(g). When the dissolved CO_2 is released from the solution into the air, part of the CO_2 gas forms bubbles that keep growing in the solution. Once the bubbles break, the CO_2 gas concentration suddenly increases, as indicated by the peak in Fig. 5(g). By sampling the solution with the glass capillary as

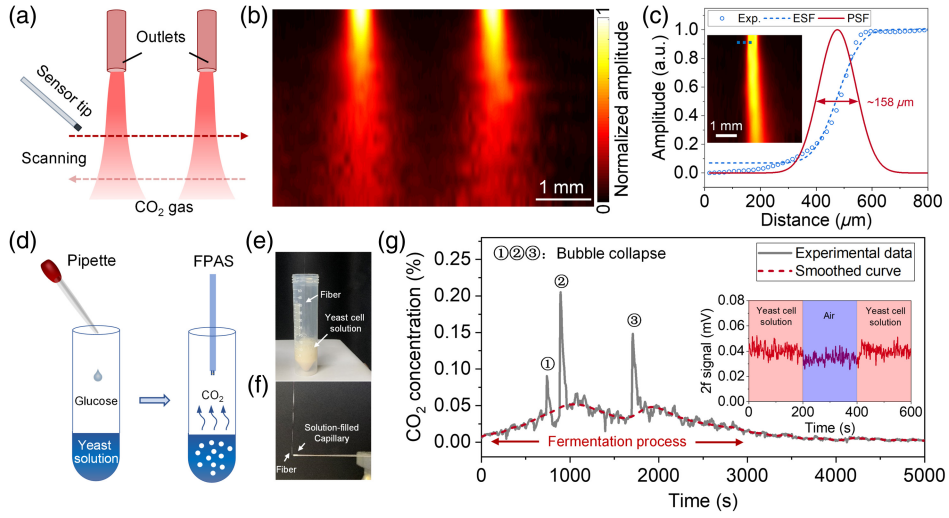

Fig. 5 (a) Schematic of 2D mapping of the CO_2 gas flow. (b) Image of the concentration distribution of the gas flow. (c) Spatial resolution of the FPAS as estimated from the edge-spread function (ESF) and the point spread function (PSF) curves. (d) Schematic of the procedure to monitor the fermentation process of the yeast solution. Photograph of the yeast solution in (e) a test tube and (f) a glass capillary. (g) Temporal variation of the CO_2 concentration. The dashed line is the smooth curve with a window of 30 points to clearly show the concentration evolution. Inset: Peak value of the 2f signal for the CO_2 released from ~100 nL yeast solution. Exp., experimental.

shown in Fig. 5(f), the FPAS with an equivalent gas cell volume of ~260 pL is capable of detecting the fermentation solution with a volume down to ~100 nL, as shown in the inset of Fig. 5(g).

2.7 In vivo Intravascular Dissolved Gas Monitoring

As the absorption line of the CO_2 at the middle-infrared band is approximately 2 orders of magnitude stronger than that at the near-infrared wavelength of 1578 nm according to the HITRAN database,[40] a thulium-doped fiber laser with the operation wavelength at 2006 nm is home-built (Supplementary Material Note 10) to demonstrate the capability of the FPAS to work with mid-infrared laser sources. To also showcase the potential for *in situ* dissolved gas monitoring in an extremely narrow space, instead of just the gas-phase measurement, the FPAS after being encapsulated into a permeable polymer tube is demonstrated for dissolved CO_2 monitoring in the rat blood vessel, as shown in Fig. 6(a). Before the animal test, the performance of the FPAS for the dissolved CO_2 measurement is studied by inserting the FPAS into the distilled water saturated with the CO_2 gas of different concentrations from 1% to 5%. A good linear response is observed in Fig. 6(b). The temporary response of the FPAS to

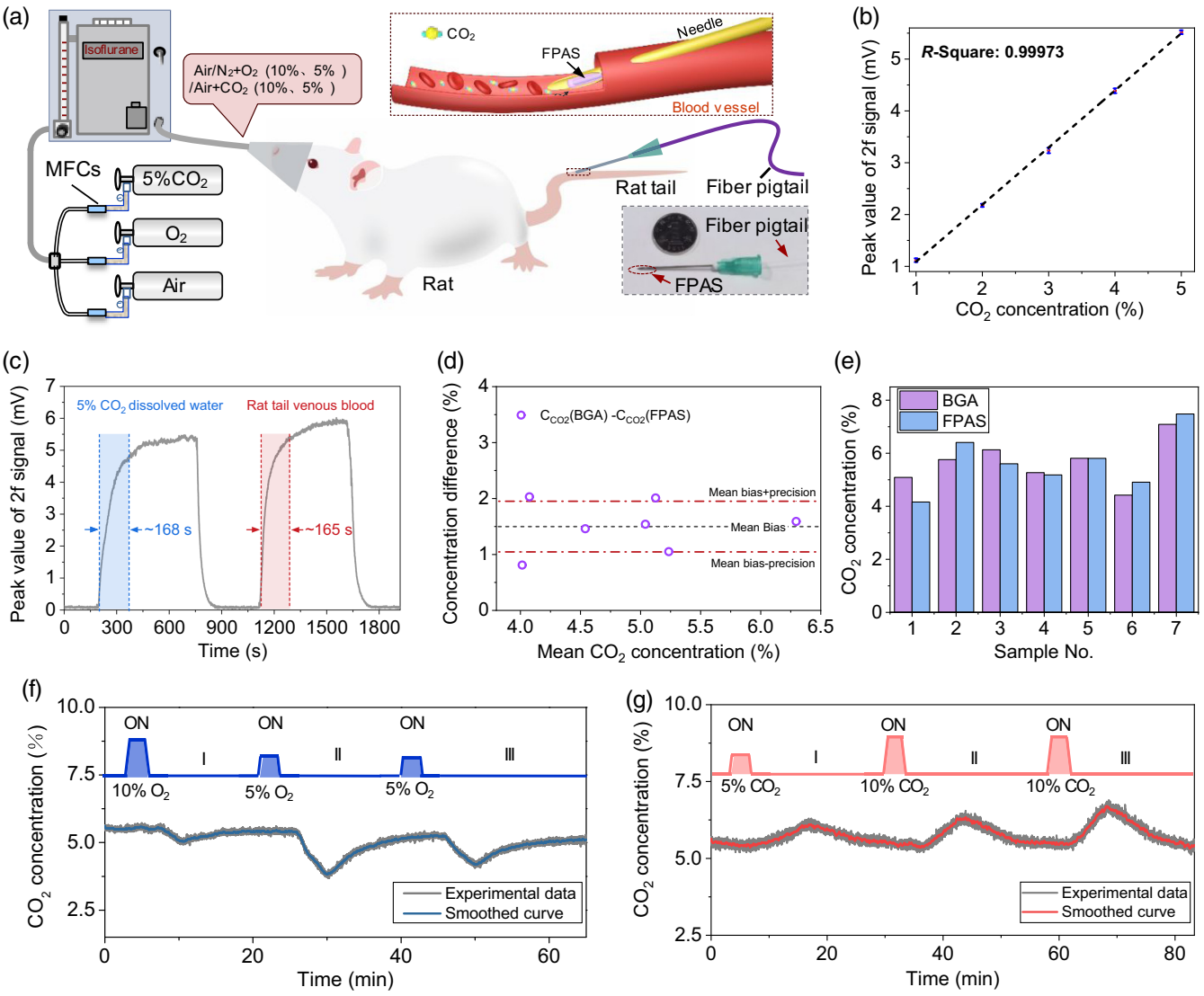

Fig. 6 (a) Schematic of *in vivo* monitoring of the dissolved CO_2 gas in a rat tail vein. Inset: schematic of the FPAS inserted into the rat tail vein and photograph of the FPAS inserted in a 21G syringe needle. (b) Peak value of the 2f signal from the FPAS versus the concentration of the dissolved CO_2 in the water. (c) Temporal response of the FPAS inserted into 5% CO_2 dissolved water and the blood sample from the rat tail vein. (d) The bias, or difference of the paired CO_2 concentration (C_{CO2}), as a function of the mean value measured by the blood gas analyzer (BGA) and the FPAS. (e) Histogram of the C_{CO2} values measured by the BGA and the FPAS for seven rat tail blood samples. Real-time *in vivo* monitoring of the rat intravascular C_{CO2} in (f) the hypoxia conditions (5% and 10% O_2) and (g) the hypercapnic conditions (5% and 10% CO_2). The measured data are smoothed with a window of 30 points to show the dynamic concentration change more clearly.

5% dissolved CO_2 is also measured, as shown in Fig. 6(c). The response time, defined as the rising time for the signal from 10% to 90% of its maximum, is ~168 s. The longer response time compared with that in the air is caused by the permeation time of the dissolved gas into the polymer tube. The NEC for the dissolved CO_2 gas using a laser power of ~10 mW is estimated to be ~187.5 ppm (1σ noise: ~20.6 μV). The FPAS is subsequently pulled out from the water. After the CO_2 gas fully diffuses out from the tube into the ambient air, the FPAS is inserted into the blood sample drawn from a rat tail vein. The FPAS shows a similar response time in the blood sample compared with the CO_2-dissolved water. The CO_2 concentration in the blood of the rat tail vein as estimated based on the result for the 5% CO_2-dissolved water is ~5.5%.

Blood samples from the tail veins of seven rats are acquired to test the dissolved CO_2 by the blood gas analyzer (BGA) and the FPAS *in vitro*. To compare the results from two different measurement techniques, a statistical method for assessing the data using bias and precision is adopted, as Bland and Altman[41] have shown. As shown in Fig. 6(d), the measured CO_2 concentration (C_{CO2}) from the BGA and the FPAS is represented by plotting the bias, or difference of the paired data, as a function of the mean value obtained from the two different methods. The mean bias is commonly claimed as the systematic error that causes consistent over/underestimation of the C_{CO2} compared with the true value, which can be corrected by recalibrating the device. The standard deviation (SD) of the bias represents the random error of the device. After correcting the means bias, the measured C_{CO2} values in the blood samples by the two methods are compared in Fig. 6(e) and show good agreement, with a difference of less than 1%.

For *in vivo* monitoring of the C_{CO2} in the rat tail vein, the encapsulated FPAS under the assistance of a syringe needle is inserted into the rat vein (Supplementary Material Note 11). The peak values of the 2f signals are continuously recorded, and the signal amplitude continues to increase during the diffusion process of the dissolved CO_2 gas from the blood into the tube. By cyclically switching the air to a gas mixture with the reduced oxygen (O_2) to mimic the hypoxia condition, the concentration of the dissolved CO_2 in the blood of the rat reduces accordingly, as shown in Fig. 6(f). In the first cycle, a gas mixture of 10% O_2 and 90% nitrogen (N_2) is applied and the dissolved CO_2 concentration measured by the FPAS gradually reduces. In the second and third cycles, a gas mixture of 5% O_2 and 95% N_2 corresponding to a more intensive hypoxia condition results in a larger reduction in the dissolved CO_2 concentration. We further test the rat under the hypercapnic condition by cyclically applying gas mixtures with a CO_2 concentration higher than that in the air. As shown in Fig. 6(g), the dissolved CO_2 concentration also varies under the different hypercapnic conditions, and the rise of the dissolved CO_2 concentration is larger for the gas mixture with 10% CO_2 than that with 5% CO_2. In addition to the CO_2, O_2 is another important gas for clinic blood gas analysis. Based on the absorption coefficient (~0.0013 cm^{-1}) near the wavelength of 760 nm from HITRAN,[40] the corresponding detection limit of O_2 for a 10 mW pump power can be predicted to be ~250 ppm based on the measured result for the C_2H_2. Therefore, by integrating with a 760.8-nm semiconductor laser, the FPAS can serve as a promising strategy for *in vivo* continuous blood gas monitoring, avoiding the need for frequent blood sampling in applications such as early diagnosis of septic shock and monitoring of myocardial infarction and stroke.

3 Discussion

The performance of recently reported compact PAS systems based on different types of microphones is compared in terms of the system size, NEC, NNEA, and response time in Table 1. In general, the FPAS without the need for additional resonant gas cell exhibits a comparable NNEA on the level of 10^{-9} cm^{-1} W $Hz^{-1/2}$ with the large-sized or benchtop PAS systems and has a microscale footprint featuring more than 3 orders of magnitude smaller sampling volume and shorter response time.

In addition to the above PAS system, surface-enhanced spectroscopies, including surface-enhanced Raman scattering (SERS) and surface-enhanced infrared absorption spectroscopy (SEIRAS), have achieved a low detection limit down to the ppb level and even single molecule as a result of the electrical field enhanced by the several orders of magnitude.[47,48] Although previous fiber-tip SERS has been mostly used in aqueous environments for biological cells or molecule detection, few works have been reported for trace gas sensing, according to the best of our knowledge. The possible reason is the low density of gases and the high surface selectivity of the SERS or SEIRAS, which causes very few gas molecules per unit volume in the vicinity of the spatially localized electric field for detection. This also increases the response time, which is largely determined by the

Table 1 Performance comparison with small-footprint PAS systems.

Microphone type	Wavelength (nm)	Dimension (mm × mm × mm)	Integration time (s)	NEC (ppb)	NNEA (cm^{-1} W $Hz^{-1/2}$)	Response time (s)
MEMS	450[42]	120 × 65 × 35	1	0.86	2.0×10^{-8}	Not stated
Tuning fork	1531.59[43]	21 × 12.7 × 8.5	0.1	84	4.1×10^{-9}	Not stated
Optical cantilever	1530.37[23]	1.6 × 3 × 7	0.3	550	2.5×10^{-7}[a]	~100
	1532.83[44]	>5 (diameter)	1	20	2.3×10^{-9}	11.2
	1530.37[45]	2.4 × 2.4 × 14	1	24.7	1.3×10^{-9}	30
Fabry-Perot cavity	1531.59[39]	6 (diameter)	1	0.87	2.9×10^{-9}[a]	Not stated
	1530.37[46]	2.75 × 2.75 × 3	10	4300	4.4×10^{-7}[a]	Not stated
	1532.83 (this work)	0.125 × 0.125 × 0.06	1	61.2	6.1×10^{-9}	~0.02

[a]0.833 Hz bandwidth is used to estimate the NNEA based on the model of the adopted lock-in amplifier.

probability of the target sticking to the SERS substrate surface. Thus, proper surface functionalization is normally used to capture the gas molecules into the "hot spots" of the plasmonic nanostructures for ppb to ppm detection of volatile organic compounds (VOCs) and toxic gases such as hydrogen sulfide (H_2S).[49,50] On the other hand, mid-infrared (MIR) spectroscopies can realize high-sensitivity gas molecule detection owing to the strong gas absorption, approximately 2 to 3 orders of magnitude higher than that in the near-infrared band. However, the laser sources and detectors are expensive and normally need cooling to achieve high detection efficiency. The free-space light transmission and bulky gas cell also compromise the flexibility and compactness of the spectroscopy. To avoid the use of cooled semiconductor detectors, an MIR-perturbed SERS detects the Raman signals at visible wavelengths altered by MIR light absorbed in molecular bonds and exhibits the potential for single-molecule detection.[51] For the free-space transmission and bulky gas cell, low-confinement Si photonic waveguides with a short length of a few centimeters are developed for mid-infrared light, with the wavelength varying from ~2.6 to ~4.2 μm, which realizes sub-ppm to ppm detection of trace gas including CO_2, C_2H_2, and methane (CH_4) due to the high evanescent field confinement factor.[52–54] A performance comparison of the FPAS with the other advanced techniques such as SERS, SEIRAS, and waveguide-based middle-infrared spectroscopy has been provided (see Supplementary Material Note 12).

In comparison, the reported miniaturized all-in-one FPAS works in the near-infrared band, which allows the use of low-cost DFB laser sources with fiber pigtails and thus easy integration with the commercial telecom fiber, which makes the spectroscopy low-cost, miniature, and flexible. The miniaturized FPAS built at the optical fiber tip with a small diameter of 125 μm also enables a fast response of 20 ms and a small sample volume of 260 pL. From the aspect of sensitivity, considering that the gas molecules have much weaker absorption in the near-infrared than in the middle-infrared band, the local signal amplification by the microscale cavity and the acoustic-sensitive membrane demodulated by high-sensitivity fiber interferometry can effectively compensate for the sensitivity loss caused by the weak near-infrared absorption, which results in a low detection limit of 9 ppb.

Considering the broadband acoustic response of the FPAS, operation at the kilohertz range gives the FPAS a better SNR or a lower NEC, which is preferred for applications detecting low-concentration gas. By contrast, at the resonant frequency, despite the relatively lower SNR, the working frequency up to megahertz is beneficial to increase the immunity of the FPAS to low-frequency environmental noise. This broad bandwidth also allows the study of the relaxation time for diverse gas molecules such as C_2H_2 and CO_2.[55] Gas detection specificity is also important in practical applications. As the FPAS measures a specific gas based on its fingerprint spectrum, which commonly has quite narrow (several to tens of picometers) absorption peaks, two different gases without an overlapped absorption band have individual absorption lines. Thus, each gas can be measured with high specificity by aligning the pump laser wavelength to its absorption line. In case the mixed gas with multiple species has an overlapped absorption band, the principal component analysis and/or deep learning can be used for the multi-gas analysis.[56,57] The NEC of the FPAS can be further reduced using a high-power laser source to several hundreds of milliwatts or even watts. Currently, a 50 mW pump power is used because it is found that a further increase of the pump power is accompanied by the raised background signal caused by the membrane absorption. In addition, the thermal effect also degrades the membrane stability, reflecting the slight fluctuations of the reflection spectrum. One potential solution is to adopt a 45-deg-angled fiber tip aligned with the FPAS to reflect the light into the cavity.[58] Then, the pump light can pass through the cavity instead of the membrane, allowing stable detection of the gas with a much higher pump power and the extension of the pump wavelength range. Another potential direction for improving the FPAS performance is to construct a high-finesse F–P cavity. This can be implemented by replacing the polymer membrane with a high-reflectivity dielectric film or photonic crystal slab and simultaneously optimizing the parameters for coating the fiber end facet with high-reflectivity metal films without degrading the membrane's acoustic performance.[59,60] Because the absorption of the gas molecules in the middle-infrared band is several orders of magnitude larger than that in the near-infrared band, integration of the hollow core antiresonant fiber that supports efficient transmission of the middle infrared light is an interesting research direction to further improve the sensitivity of the FPAS.[61] In summary, by merging the advantages of PAS with fiber-optic interferometry, an all-fiber PAS with a microscale footprint, high spatiotemporal resolution, and minute sample volume is realized and provides a miniaturized, directly fiber-coupled, lightweight, and robust platform for real-time and *in situ* trace gas measurement in various fields such as industry process monitoring, leakage gas detection, and biopharmacy.

4 Materials and Methods

4.1 FPAS Fabrication

The fabrication process of the sensor is as follows (Supplementary Material Note 1). The fiber-tip structure is fabricated by first splicing a standard SMF (SMF28, Corning Incorporated, Corning, United States) with a piece of pure silica capillary (TSP075150, Polymicro Technologies, Phoenix, United States) using a fusion splicer (FSM-45PM, Fujikura Ltd., Tokyo, Japan) and then cleaving the capillary under microscope with a standard fiber cleaver. The capillary has an outer diameter of 126 μm and an inner bore size of 75 μm. The splicing current and time of the splicer are set to 13 bits and 90 ms, respectively. The cleaving distance from the splicing joint is controlled via a mechanical translation stage. The fiber structure is then deposited with a 4-nm-thick Au film with an ion sputter (SBC-12, KYKY Technology Co., Ltd., Beijing, China) to slightly increase the light absorption for subsequent photothermal preparation of the membrane. A minute amount of UV-curable adhesive is then dropped into the capillary using another cleaved fiber tip. Heating light from a 980 nm continuous wave (CW) laser with a power of 15 mW is coupled into the fiber through the distal fiber pigtail and absorbed by the Au film. The generated heat causes the expansion of the air trapped into the capillary, and the isotropic pressure difference induced by the air expansion drives the liquid adhesive toward the opening of the capillary. The pressure difference pneumatically squeezes the adhesive into an ultrathin membrane. Once the adhesive reaches a steady state after heating for 5 min, light from a UV lamp is used to presolidify the adhesive for several seconds. The adhesive after this presolidification forms a suspended elastic thin membrane sealing the capillary, with the thickness controlled by the volume of the dropped adhesive and the heating

power. Once the heating power is turned off, the inverse pressure difference stretches the suspended membrane. After further UV light illumination for several hours to fully solidify the adhesive, the biconcave membrane with a thickness larger at the periphery of the capillary is obtained.

4.2 Laser Patterning

Femtosecond laser pulses (Libra-USP-HE, Coherent Inc., Saxonburg, United States) with a repetition rate of 1 kHz and an average power of 0.7 mW are focused by an objective with an NA of 0.4 to pattern the membrane. The fiber tip is faced upright toward the objective. Once the laser spot is focused onto the membrane surface, the fiber tip is moved by a 2D translation stage (M-VP-25XL, Newport Corporation, Irvine, United States) driven by a programmable controller. By inscribing four evenly distributed arcs along the azimuthal direction near the membrane edges, four holes are cut in the membrane (Supplementary Material Note 1). The step size and the moving speed of the translation stage are 0.45 μm and 14 μm/s, respectively.

4.3 Acoustic and PA Gas Test

The frequency response of the FPAS to acoustic waves at the frequency from 1 to 20 kHz is acquired by measuring the intensity change of the reflected probe light. The probe light from a tunable laser (CoBrite DX1, ID Photonics GmbH, Neubiberg, Germany) after traveling through an optical circulator reaches the FPAS. The reflected probe light from the FPAS after passing through the circulator is converted to electrical signals by a photodiode (2053-FC, PD, New Focus, Irvine, United States) and acquired by an oscillator (PicoScope 5244B, Pico Technology, Tyler, United States). The acoustic waves are generated from a loudspeaker driven by a signal generator and calibrated with a standard microphone (AWA5661, Aihua Instrument, Hangzhou, China). The NEP is obtained using an electrical spectrum analyzer (FSV300, R&S, Munich, Germany) to measure the SNR. Both the FPAS and the microphone are placed in an acoustic isolation box and positioned symmetrically along the central axis of the loudspeaker.

The FPAS is placed into a gas chamber, where the sample gas is injected through the inset continuously at a constant flow rate of 100 sccm. The gas concentration is controlled by two mass flow controllers (MFCs) that regulate the flow rate of the sample gas and N_2. Pump light from DFB laser sources at 1532, 1578, and 2006 nm is coupled with the probe light via optical couplers [see Fig. 3(a)] to excite the PA signals from the C_2H_2 and CO_2 gas. The pump light at 1532 and 1578 nm is amplified by an EDFA (C-BA-20/L-BA-23, MRX-RRY Photonics, Hefei, China), and the pump light at 2006 nm is amplified by a home-built thulium-doped fiber amplifier (Supplementary Material Note 10). The wavelength of the pump light is scanned over the gas absorption line and modulated sinusoidally by controlling the laser temperature and driving current, respectively (LDC205C/TED200C, Thorlabs, Newton, United States). To maximize the 2f signal, the modulation depth of the pump light wavelength is set to ~2.2 times the absorption half linewidth, corresponding to a sinusoidal modulation voltage of 250 and 270 mV for the C_2H_2 and CO_2 sensing, respectively, at a modulation frequency of 7 kHz. The probe light with a wavelength of ~1550 nm and a power of ~5.4 mW is reflected from the FPAS after traveling through the coupler, and the circulator is converted into the electrical signal by the PD. A bandpass filter with a center wavelength of 1550 nm and a bandwidth of 15 nm is added before the PD to filter off the residual pump light. The output signal from the PD is received by a lock-in amplifier (ziHF2, Zurich Instruments, Zürich, Switzerland) with a filter slope of 18 dB/Oct and a time constant of 0.1 s. For continuous monitoring, the pump light wavelength is fixed at the absorption line instead of being slowly scanned; then the peak values of the 2f signals are recorded.

4.4 Air Flow Imaging

CO_2 gas with a concentration of 5% is injected into a multichannel shunt needle to form separate gas flows. Each channel has an inner diameter of ~0.26 mm. The gas flow rate is set to 40 sccm. The FPAS is mounted onto a 2D translation stage (ML01.8A1, PI, Karlsruhe, Germany) with the fiber tip facing downward to avoid possible disturbance caused by the airflow. To avoid gas-flow-induced fiber swaying, the suspended fiber tip has a short length of ~4 mm. During the gas flow mapping process, the FPAS is scanned crossing the horizontal gas channels with a translation speed of 0.3 mm/s for a distance of 20 mm. To characterize the spatial resolution, the CO_2 gas is injected into a needle with an inner diameter of 0.06 mm.

4.5 Monitoring Fermentation of Yeast Cells

The yeast cell is cultivated in a test tube with an inner diameter of 2.7 cm. 250 mg yeast powder is added to 5 mL pure water and stirred to obtain a 0.05 g/mL yeast solution. A 1 mL glucose solution with a concentration of 0.12 g/mL is then added to the yeast solution. With the assistance of a linear translation stage, the FPAS is immediately inserted into the test tube and keeps a distance of 5 cm from the solution surface to prevent it from contacting the foams produced during the fermentation. The generated CO_2 gas during the fermentation process is released to the headspace of the yeast solution and is continuously monitored over a period of ~1.5 h. To sample the yeast cell solution with a nanoliter-scale volume, a glass capillary as a micropipette is used for sampling. One end of the capillary is sealed with epoxy to trap the tiny droplet drawn inside the capillary and thus avoid direct exposure to the ambient air for slow evaporation. Using a glass capillary with a 0.3-mm bore diameter, the yeast solution filling the capillary with a length of 1.45 mm has a volume of ~100 nL.

4.6 In Vivo Analysis of Intravascular Dissolved CO_2 in the Rat

The dissolved CO_2 in blood samples from the rat tail vein is tested by a blood gas analyzer (BGA, i15VET, EDAN Instruments, Shenzhen, China). Part of the blood sample is tested by the FPAS at the same time. The FPAS is encapsulated into a thin-wall Teflon permeable tube with a bore diameter of ~250 μm and an outer diameter of ~510 μm (AF 2400 tubing, Teflon™, Wilmington, United States) before immersing into the blood samples. For *in vivo* dissolved CO_2 monitoring, after the rat in a homemade chamber is anesthetized with isoflurane, a medical syringe needle (21G) is punctured into the tail vein. The tube-encapsulated FPAS is carefully inserted into the vein through the needle. The needle and the fiber pigtail are then fixed by the medical tapes. To avoid blood coagulation, which causes an unusual increase in the CO_2 gas concentration, the injection needle before inserting into the rat blood vessel is

treated with sodium heparin solution (0.1%, 12.5 KU, Yuanye Bio-Technology, Shanghai, China) in advance. The gas mixture of O_2/N_2 or air/CO_2 is injected into the chamber to monitor the dynamic change of the intravascular dissolved CO_2 concentration in the rat vein by the FPAS. All procedures for the animal experiment are carried out in accordance with the Institutional Animal Care and Use Committee at Jinan University.

Disclosures

The authors declare no conflicts of interest.

Code and Data Availability

Data underlying the results presented in this paper have been provided within the main text and Supplementary Material. All the other data that support the findings of this study are available from the corresponding authors upon reasonable request.

Acknowledgements

This work was supported by the National Natural Science Foundation of China (Grant Nos. 62275106 and 62135006), the Local Innovative and Research Teams Project of Guangdong Pearl River Talents Program (Grant No. 2019BT02X105), the Natural Science Foundation of Guangdong Province (Grant Nos. 2022A1515010105 and 2023A1515011415), and the Doctoral Students Top Innovative Talent Training Program of Jinan University (Grant No. 2023CXB016).

References

1. J. Hodgkinson and R. P. Tatam, "Optical gas sensing: a review," *Meas. Sci. Technol.* **24**(1), 012004 (2012).
2. C. P. Bacon, Y. Mattley, and R. DeFrece, "Miniature spectroscopic instrumentation: applications to biology and chemistry," *Rev. Sci. Instrum.* **75**(1), 1–16 (2004).
3. R. A. Crocombe, "Portable spectroscopy," *Appl. Spectrosc.* **72**(12), 1701–1751 (2018).
4. A. Maity, S. Maithani, and M. Pradhan, "Cavity ring-down spectroscopy: recent technological advancements, techniques, and applications," *Anal. Chem.* **93**(1), 388–416 (2020).
5. P. Wang et al, "A review of cavity-enhanced Raman spectroscopy as a gas sensing method," *Appl. Spectrosc. Rev.* **55**(5), 393–417 (2020).
6. A. Fathy et al, "Direct absorption and photoacoustic spectroscopy for gas sensing and analysis: a critical review," *Laser Photonics Rev.* **16**(8), 2100556 (2022).
7. X. Ren et al., "Dual-comb optomechanical spectroscopy," *Nat. Commun.* **14**(1), 5037 (2023).
8. W. Jin et al., "Ultra-sensitive all-fibre photothermal spectroscopy with large dynamic range," *Nat. Commun.* **6**(1), 6767 (2015).
9. R. M. Wynne et al., "Sub-minute response time of a hollow-core photonic bandgap fiber gas sensor," *J. Lightwave Technol.* **27**, 1590–1596 (2009).
10. P. Zhao et al., "Mode-phase-difference photothermal spectroscopy for gas detection with an anti-resonant hollow-core optical fiber," *Nat. Commun.* **11**(1), 847 (2020).
11. L. Tombez et al., "Methane absorption spectroscopy on a silicon photonic chip," *Optica* **4**(11), 1322–1325 (2017).
12. M. Lafuente et al., "On-chip monitoring of toxic gases: capture and label-free SERS detection with plasmonic mesoporous sorbents," *Lab Chip* **23**(14), 3160–3171 (2023).
13. M. G. Suh et al., "Microresonator soliton dual-comb spectroscopy," *Science* **354**(6312), 600–603 (2016).
14. D. Grassani et al., "Mid infrared gas spectroscopy using efficient fiber laser driven photonic chip-based supercontinuum," *Nat. Commun.* **10**(1), 1553 (2019).
15. F. Harren et al., "Photoacoustic spectroscopy in trace gas monitoring," *Encycl. Anal. Chem.* **3**, 2203–2226 (2000).
16. P. Patimisco et al., "Recent advances in quartz enhanced photoacoustic sensing," *Appl. Phys. Rev.* **5**(1), 011106 (2018).
17. L. Xiong et al., "Photoacoustic trace detection of gases at the parts-per-quadrillion level with a moving optical grating," *Proc. Natl. Acad. Sci. U. S. A.* **114**(28), 7246–7249 (2017).
18. R. Bauer et al., "3D-printed miniature gas cell for photoacoustic spectroscopy of trace gases," *Opt. Lett.* **39**(16), 4796–4799 (2014).
19. J. Karhu et al., "Sub-ppb detection of benzene using cantilever-enhanced photoacoustic spectroscopy with a long-wavelength infrared quantum cascade laser," *Opt. Lett.* **45**(21), 5962–5965 (2020).
20. Y. Tan et al., "Optical fiber photoacoustic gas sensor with graphene nano-mechanical resonator as the acoustic detector," *IEEE J. Sel. Top. Quantum Electron.* **23**(2), 199–209 (2016).
21. H. Xiao et al., "Ultra-sensitive ppb-level methane detection based on NIR all-optical photoacoustic spectroscopy by using differential fiber-optic microphones with gold-chromium composite nanomembrane," *Photoacoustics* **26**, 100353 (2022).
22. C. Zhang et al., "All-optical fiber photoacoustic gas sensor with double resonant enhancement," *IEEE Photonics Technol. Lett.* **30**(20), 1752–1755 (2018).
23. G. Gruca et al., "Demonstration of a miniature all-optical photoacoustic spectrometer based on ferrule-top technology," *Opt. Lett.* **38**(10), 1672–1674 (2013).
24. E. Fan et al., "Compact optical fiber photoacoustic gas sensor with integrated multi-pass cell," *Photoacoustics* **32**, 100524 (2023).
25. R. Cui et al., "Three-dimensional printed miniature fiber-coupled multipass cells with dense spot patterns for ppb-level methane detection using a near-IR diode laser," *Anal. Chem.* **92**(19), 13034–13041 (2020).
26. Y. Zhang et al., "Continuous real-time monitoring of carbon dioxide emitted from human skin by quartz-enhanced photoacoustic spectroscopy," *Photoacoustics* **30**, 100488 (2023).
27. C. Li et al., "Miniature single-fiber photoacoustic sensor for methane gas leakage detection," *Opt. Lasers Eng.* **149**, 106792 (2022).
28. T. Martins et al., "Fiber-integrated phase change metasurfaces with switchable group delay dispersion," *Adv. Opt. Mater.* **9**(21), 2100803 (2021).
29. E. A. Chan et al., "Plasmono-atomic interactions on a fiber tip," *Appl. Phys. Lett.* **116**(18), 183101 (2020).
30. E. J. Smythe et al., "Optical antenna arrays on a fiber facet for *in situ* surface-enhanced Raman scattering detection," *Nano Lett.* **9**(3), 1132–1138 (2009).
31. V. Melissinaki et al., "A fiber-endface, Fabry–Perot vapor microsensor fabricated by multiphoton polymerization," *IEEE J. Sel. Top. Quantum Electron.* **21**(4), 344–353 (2015).
32. L.-L. Lai et al., "3D printing of glass micro-optics with subwavelength features on optical fiber tips," *ACS Nano* **18**(16), 10788–10797 (2024).
33. O. Kilic et al., "Miniature photonic-crystal hydrophone optimized for ocean acoustics," *J. Acoust. Soc. Am.* **129**(4), 1837–1850 (2011).
34. J. Ma et al., "Fiber-optic Fabry–Pérot acoustic sensor with multilayer graphene diaphragm," *IEEE Photonics Technol. Lett.* **25**(10), 932–935 (2013).
35. A. Rosencwaig, *Photoacoustics and Photoacoustic Spectroscopy*, Wiley and Sons, Chichester (1980).
36. T. Kuusela and J. Kauppinen, "Photoacoustic gas analysis using interferometric cantilever microphone," *Appl. Spectrosc. Rev.* **42**(5), 443–474 (2007).
37. H. Wu et al., "Beat frequency quartz-enhanced photoacoustic spectroscopy for fast and calibration-free continuous trace-gas monitoring," *Nat. Commun.* **8**(1), 15331 (2017).
38. K. Chen et al., "Ultra-high sensitive fiber-optic Fabry-Perot cantilever enhanced resonant photoacoustic spectroscopy," *Sens. Actuators B-Chem.* **268**, 205–209 (2018).

39. Z. Gong et al., "High-sensitivity fiber-optic acoustic sensor for photoacoustic spectroscopy based traces gas detection," *Sens. Actuators B-Chem.* **247**, 290–295 (2017).
40. I. E. Gordon et al., "The HITRAN2020 molecular spectroscopic database," *J. Quantum Spectrosc. Radiat. Transf.* **277**, 107949 (2022).
41. J. M. Bland and D. Altman, "Statistical methods for assessing agreement between two methods of clinical measurement," *Lancet* **327**(8476), 307–310 (1986).
42. Y. Dong et al., "Fully integrated photoacoustic NO_2 sensor for sub-ppb level measurement," *Sensors* **20**(5), 1270 (2020).
43. L. Dong et al., "QEPAS spectrophones: design, optimization, and performance," *Appl. Phys. B* **100**(3), 627–635 (2010).
44. K. Chen et al., "Fiber-optic photoacoustic sensor for remote monitoring of gas micro-leakage," *Opt. Express* **27**(4), 4648–4659 (2019).
45. S. Zhou and D. Iannuzzi, "A fiber-tip photoacoustic sensor for *in situ* trace gas detection," *Rev. Sci. Instrum.* **90**(2), 023102 (2019).
46. Y. Cao et al., "Miniature fiber-tip photoacoustic spectrometer for trace gas detection," *Opt. Lett.* **38**(4), 434–436 (2013).
47. L. M. Liz-Marzán et al., "Fifty years of surface-enhanced spectroscopy," *ACS Nano* **18**(8), 5995–5997 (2024).
48. F. Neubrech et al., "Surface-enhanced infrared spectroscopy using resonant nanoantennas," *Chem. Rev.* **117**(7), 5110–5145 (2017).
49. K. Kant et al., "Plasmonic nanoparticle sensors: current progress, challenges, and future prospects," *Nanosc. Horiz.* **9**(12), 2085–2166 (2024).
50. J. Wang et al., "Surface-enhanced infrared absorption spectroscopy (SEIRAS) for biochemical analysis: progress and perspective," *Trends Environ. Anal. Chem.* **41**, e00226 (2024).
51. R. Chikkaraddy et al., "Mid-infrared-perturbed molecular vibrational signatures in plasmonic nanocavities," *Light Sci. Appl.* **11**(1), 19 (2022).
52. F. Ottonello-Briano et al., "Carbon dioxide absorption spectroscopy with a mid-infrared silicon photonic waveguide," *Opt. Lett.* **45**(1), 109–112 (2020).
53. M. Vlk et al., "Extraordinary evanescent field confinement waveguide sensor for mid-infrared trace gas spectroscopy," *Light Sci. Appl.* **10**(1), 26 (2021).
54. H. D. Yallew et al., "Sub-ppm methane detection with mid-infrared slot waveguides," *ACS Photonics* **10**(12), 4282–4289 (2023).
55. S. D. Russo et al., "Quartz-enhanced photoacoustic spectroscopy exploiting low-frequency tuning forks as a tool to measure the vibrational relaxation rate in gas species," *Photoacoustics* **21**, 100227 (2021).
56. S. X. Leong et al., "Enantiospecific molecular fingerprinting using potential-modulated surface-enhanced Raman scattering to achieve label-free chiral differentiation," *ACS Nano* **15**(1), 1817–1825 (2021).
57. M. Kang et al., "High accuracy real-time multi-gas identification by a batch-uniform gas sensor array and deep learning algorithm," *ACS Sens.* **7**(2), 430–440 (2022).
58. H. Bae et al., "Miniature surface-mountable Fabry–Perot pressure sensor constructed with a 45 angled fiber," *Opt. Lett.* **35**(10), 1701–1703 (2010).
59. O. Kilic et al., "External fibre Fabry–Perot acoustic sensor based on a photonic-crystal mirror," *Meas. Sci. Technol.* **18**(10), 3049 (2007).
60. J. A. Guggenheim et al., "Ultrasensitive plano-concave optical microresonators for ultrasound sensing," *Nat. Photonics* **11**(11), 714–719 (2017).
61. D. Tomaszewska-Rolla et al., "Mid-infrared optical frequency comb spectroscopy using an all-silica antiresonant hollow-core fiber," *Opt. Express* **32**(6), 10679–10689 (2024).
62. C. L. Lee et al., "Highly sensitive air-gap fiber Fabry–Pérot interferometers based on polymer-filled hollow core fibers," *IEEE Photonics Technol. Lett.* **24**(2), 149–151 (2012).
63. T. Mellow and L. Kärkkäinen, "On the sound field of an oscillating disk in a finite open and closed circular baffle," *J. Acoust. Soc. Am.* **118**(3), 1311–1325 (2005).
64. W. Xiong et al., "Sensitivity enhanced fiber optic hydrophone based on an extrinsic Fabry-Perot interferometer for low-frequency underwater acoustic sensing," *Opt. Express* **30**(6), 9307–9320 (2022).
65. Y. L. Hoo et al., "Design and modeling of a photonic crystal fiber gas sensor," *Appl. Opt.* **42**(18), 3509–3515 (2003).
66. Y. Shi and J. Fang, "Yolk–shell hierarchical pore Au@MOF nanostructures: efficient gas capture and enrichment for advanced breath analysis," *Nano Lett.* **24**(33), 10139–10147 (2024).
67. Z. Zhao et al., "Efficient SERS response of porous-ZnO-covered gold nanoarray chips to trace benzene–volatile organic compounds," *ACS Appl. Mater. Interfaces* **14**(42), 47999–48010 (2022).
68. Y. Liu et al., "Facile all-optical method for *in situ* detection of low amounts of ammonia," *iScience* **23**(11), 101757 (2020).
69. H. Fu et al., "Ultrathin hexagonal PbO nanosheets induced by laser ablation in water for chemically trapping surface-enhanced Raman spectroscopy chips and detection of trace gaseous H_2S," *ACS Appl. Mater. Interfaces* **12**(20), 23330–23339 (2020).
70. C. Awada et al., "Detection of hot electron-driven photochemical reaction of steady-state NO_2 gas molecules by surface–enhanced Raman spectroscopy," *Appl. Surf. Sci.* **604**, 154577 (2022).
71. H. Zhou et al., "Metal–organic framework-surface-enhanced infrared absorption platform enables simultaneous on-chip sensing of greenhouse gases," *Adv. Sci.* **7**(20), 2001173 (2020).
72. D. Hasan and C. Lee, "Hybrid metamaterial absorber platform for sensing of CO_2 gas at mid-IR," *Adv. Sci.* **5**(5), 1700581 (2018).
73. N. J. Bareza et al., "Phonon-enhanced mid-infrared CO_2 gas sensing using boron nitride nanoresonators," *ACS Photonics* **9**(1), 34–42 (2022).

Jun Ma received his BEng degree from Huazhong University of Science and Technology, Hubei, China, in 2010, and his PhD from the Hong Kong Polytechnic University, Kowloon, Hong Kong, in 2014. From 2015 to 2016, he was a postdoctoral research fellow at Washington University at St. Louis, St. Louis, MO, United States. Since 2016, he has been with the Institute of Photonics Technology, Jinan University, Guangzhou, China, as an associate professor. His current research interests include fiber-optic acoustic sensors and photoacoustic spectroscopy/imaging.

Enbo Fan is currently pursuing his PhD at the Institute of Photonics Technology, Jinan University, Guangzhou, China. His research interests include optical fiber devices and gas detection.

Haojie Liu is currently pursuing her PhD at the Institute of Photonics Technology, Jinan University, Guangzhou, China. Her research interests include optical fiber devices and fiber-optic sensors.

Yi Zhang obtained his MD degree from Jinan University and has been at the Department of Biomedical Engineering, School of Life Science and Technology, Jinan University, as an associate professor. His research interests include the multiscale construction of biomedical materials and their application in the treatment, diagnosis, and sensing of major diseases.

Cong Mai serves as the medical doctor of the Department of Emergency Medicine, Guangdong Provincial People's Hospital (Guangdong Academy of Medical Sciences), Southern Medical University, Guangdong. He has focused on the treatment and research of cardiac arrest and large vascular diseases and the treatment of brain injury after cardiac arrest.

Xin Li obtained his MD degree from Sun Yat-sen University in 2008. Currently, he serves as the vice president of Guangdong Provincial People's Hospital. He has authored more than 60 papers in SCI-indexed journals such as the *European Heart Journal*, *Bioactive Materials*,

Allergy, *Journal Nanobiotechnology*, and *Aging Cell*. Furthermore, he has published eight academic monographs, serving as editor-in-chief for six of them. Over the years, he has focused on the treatment and research of cardiac arrest and large vascular diseases and has conducted in-depth research in the pathogenesis of aortic dissection, the therapeutic effect of vascular stem cells, and the treatment of brain injury after cardiac arrest.

Wei Jin received his BEng and MSc degrees from the Beijing University of Aeronautics and Astronautics in 1984 and 1987, respectively. He received his PhD in 1991 in fiber optics from the University of Strathclyde and afterward was employed as a postdoctoral research fellow at the same university till the end of 1995. He joined the Department of Electrical Engineering of the Hong Kong Polytechnic University as an assistant professor in 1996 and was promoted to associate professor in 1998 and professor in 2003. His research interests are photonic crystal fibers and devices, optical fiber sensors, fiber lasers and amplifiers, and optical gas detectors. He is a fellow of OSA, a senior member of IEEE, and a member of SPIE.

Bai-Ou Guan received his BSc degree in applied physics from Sichuan University, Chengdu, China, in 1994, and his MSc and PhD degrees in optics from Nankai University, Tianjin, China, in 1997 and 2000, respectively. From 2000 to 2005, he was with the Department of Electrical Engineering, the Hong Kong Polytechnic University, Hong Kong, first as a Research Associate, and then as a Postdoctoral Research Fellow. From 2005 to 2009, he was with School of Physics and Optoelectronic Engineering, Dalian University of Technology, Dalian, as a full professor, where he established the PolyU-DUT Joint Research Center for Photonics. In 2009, he joined Jinan University, Guangzhou, where he founded the Institute of Photonics Technology. His current research interests include fiber optic devices and technologies, optical fiber sensors, biomedical photonic sensing and imaging, and microwave photonics. He has authored and coauthored more than 380 papers in the peer-reviewed international journals and presented 80 invited talks at international and national conferences. He received the Distinguished Young Scientist Grant from Natural Science Foundation of China (NSFC) in 2012. He is a fellow of Optica, and has served as general chair/co-chair, Technical Program Committee or Subcommittee chair/co-chair for over 30 international conferences.